Optimal Dual-Phase-Shift Control Strategy of an Isolated Buck–Boost Converter With a Clamped Inductor

Fang Li, Yan Li, *Member, IEEE*, and Xiaojie You

***Abstract*—An optimal dual-phase-shift control strategy of an isolated buck–boost converter is proposed in this paper. The theoretical analysis of dual-phase-shift control strategy is complemented, and the three-dimensional graphs of the output current versus two control variables are given. The optimal operating point is determined by the peak current of a clamped inductor and is shown as control trajectories in the three-dimensional graphs. Moreover, with the optimal dual-phase-shift control strategy, low current value, soft-switching operation, wide input voltage range regulation, whole load range regulation, and high-efficiency performance can be achieved. Furthermore, parameter design method deriving from the minimum peak current of the clamped inductor is given. At the end of this paper, a 1000 W-output prototype is fabricated to verify the effectiveness of the proposed control strategy.**

***Index Terms*—Clamped inductor, dual-phase-shift modulation, isolated buck–boost (IBB) converter, optimal control.**

I. Introduction

With the development of technology, wide input voltage range, wide range of soft-switching, high conversion efficiency and high power density are required in the unidirectional isolated dc/dc converter. Traditional phase-shifted full bridge converter has been widely used. However, it can only operate in buck mode, and has duty cycle loss and high voltage ringing on the rectifier diodes, and cannot achieve zero voltage switching (ZVS) at light load [1], [2]. *LLC* resonant converter can achieve high power density with high switching frequency and maintain soft-switching in wide load range. While the power device current stress and the circulating energy of the *LLC* converter are both very large, its transformer design is difficult in view of variable-frequency control [3], [4]. Full-bridge boost converter that cascades full-bridge and boost circuit together is proposed for wide input voltage range applications [5], [6]. Nevertheless, the volume of this converter is still large because of the existence of a dc inductor. In addition, its control strategy is also complicated.

Manuscript received January 4, 2017; revised March 17, 2017 and June 5, 2017; accepted July 11, 2017. Date of publication July 27, 2017; date of current version February 22, 2018. This work was supported by the National Key Research and Development Program of China under Grant 2016YFE0131700. Recommended for publication by Associate Editor Yan Xing. *(Corresponding author: Yan Li.)*

The authors are with the Institute of Power Electronics, Beijing Jiaotong University, Beijing 10044, China (e-mail: hahalifang@ 163.com; liyan@bjtu.edu.cn; xjyou@bjtu.edu.cn).

Color versions of one or more of the figures in this paper are available online at http://ieeexplore.ieee.org.

Digital Object Identifier 10.1109/TPEL.2017.2732439

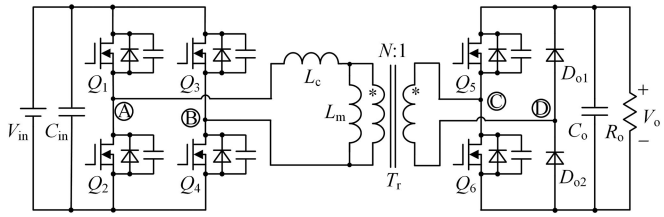

Fig. 1. Schematic of the IBB converter with a clamped inductor.

Isolated buck–boost (IBB) converter has an ac inductor in series with transformer in ac link instead of a dc inductor in input or output filters [7]–[9]. Because the current of the ac inductor changes at different voltages across it, we call the ac inductor as a clamped inductor (L_c) in this paper. IBB converter can operate either in buck or boost mode, and its advantages are listed as follows:

1) The energy storage inductor is in series with transformer, the converter may achieve higher power density. The increasing or decreasing slope of inductor current is decided by the voltage across it, and the variation of inductor current can be controlled directly such that the current stress can be limited.
2) The magnetizing inductance of ac transformer is larger than that of the *LLC* converter, so the circulating energy and conduction loss are not so large as those of the *LLC* converter.
3) Inductor current can help the soft-switching of all the switches in whole load range, and the ringing of rectifier diode is avoided inherently. Hence, the IBB converter has excellent soft-switching characteristics.

The simplified IBB converter topology is full bridge circuit with uncontrolled rectifier. Under phase-shift modulation or trailing edge pulse width modulation, the converter can only step down the input voltage by regulating the equivalent duty cycle of primary circuit [10]–[12]. Variable-frequency modulation and phase-shift with variable-frequency modulation were proposed in [13] and [14].

IBB converter with semi-active rectifier was regarded as a semi-dual-active-bridge converter, as shown in Fig. 1. With active switches in secondary rectifier, the converter can step up or step down the input voltage, and its control strategy becomes more flexible with new control variable.

Dual active bridge (DAB) converter is a special case of the IBB converter with full active rectifier [15], [16]. A lot of literature has optimized the control strategies and characteristics of a DAB converter in different aspects [17]–[19]. In particular, [20] proposed the extended dual-phase shifting-control. It must be noted that the control strategies of the DAB converter cannot be used in a semi-DAB converter directly because of the existence of second-side diodes.

In this paper, we will analyze the control strategy of the semi-DAB converter under constant-frequency control. The existing control strategies can be summarized into two categories. One can be named as single-phase-shift (SPS) modulation [21], [22]. The secondary-side switches are phase shifted from the primary square-wave. With SPS modulation, the converter can achieve ZVS of switches in both primary-side and secondary-side circuits, and can operate in buck or boost mode. The drawback of SPS modulation is that the converter cannot output low power in buck mode. The other one can be named as double-phase-shift (DPS) modulation [8], [9], [23], [24]. In boost mode, DPS modulation is the same as SPS modulation. While in buck mode, at light load only phase-shift angle of primary full bridge is regulated, at heavy load the phase-shift angles in primary and secondary bridge are both regulated. The sum of the equivalent duty cycle of the two phase-shift angles is equal to the voltage gain. With DPS modulation, the converter can achieve regulation in whole load range.

However, the SPS and DPS control strategies of the IBB converter were given straightly without the reason why this control strategy was selected. The operational principle of the IBB converter with dual-phase-shift control requires further analysis, such as the combination of control variables, power transfer capability, and so on. In this paper, we will propose optimal dual-phase-shift (ODPS) control strategy based on the criteria of optimal operating point determination.

Furthermore, the parameter design is another important involved issue. After determining the turns ratio of transformer, [7]–[9] draw the curves of normalized inductor rms currents versus normalized voltage gain in order to decide the inductance. While there are many other design considerations, such as switching frequency, transformer turns ratio, the range of input voltage, and so on, we would like to put forward a parameter design process with all of the design considerations comprehensively.

The paper is organized as follows: Section II analyzes the operational principle of dual-phase-shift modulation at different voltage gains *M*; Section III proposes the criteria for determining optimal operating point, and provides the control trajectories when at $M < 1$ or $M > 1$, and also the soft-switching performance; Section IV presents parameter design; and Section V presents experimental verification. Section VI presents the conclusion.

II. Operational Principles

The circuit topology of the IBB converter with the clamped inductor is shown in Fig. 1, the primary-side is full-bridge circuit, and the secondary-side rectifier contains Q_5 and Q_6, and D_{o1} and D_{o2}. Clamped inductor L_c includes the primary-side leakage inductance of transformer, and it is in series with the transformer T_r.

The output voltage of the IBB converter is constant. The turns ratio of transformer is *N*:1, and the magnetizing inductance of transformer L_m is infinite. We define voltage gain *M* as the ratio between NV_o and $V_{\rm in}$, i.e., $M = NV_o/V_{\rm in}$. The output voltage of primary full-bridge is v_{AB}, and the input voltage of secondary bridge is v_{CD}. Each switch has a constant duty cycle of 0.5 at the same switching frequency. In this paper, we do not consider the dead zone, suppose that $N = 1$, and all the devices are ideal to simplify the analysis.

In Fig. 2, v_{AB} changes from zero to positive level at t_0, and v_{AB} changes from zero to negative level at *T*. The time interval between t_0 and *T* is half of a period. The total switching period is $T_s = 2T$. There are two phase-shift angles of dual-phase-shift control strategy. We define the length of the time interval between t_0 and the time when v_{CD} changes from zero to positive level as D_1T, and the length of the time interval between v_{CD} changes from zero to positive level and v_{AB} changes from positive level to zero level as D_2T. Here, $D_1 + D_2 \le 1$.

At heavy load, the clamped inductor current is continuous current mode (CCM) as shown in Fig. 2(a) and (d), and we name them as mode 1 for simplicity. At medium load, the clamped inductor current is trapezoidal in discontinuous current mode (DCM) mode as shown in Fig. 2(b) and (e), and we name them as mode 2 for simplicity. At extreme light load, Fig. 2(c) shows buck-CCM mode with large circulating energy, and the clamped inductor current is triangular in boost-DCM mode as shown in Fig. 2(f). In this paper, Fig. 2(c) and (f) are unified as mode 3.

Fig. 3(a)–(d) shows the equivalent schematics of four intervals in positive half-cycle of Fig. 2(a). The negative half-cycle is similar, so we omit it.

A. Mode 1

State I [t_0, t_1]: At t_0, v_{AB} changes from zero to positive level and the current of the clamped inductor is still negative. In Fig. 3(a), during state I the current increases linearly. When the current is zero at t_1, state I ends. The length of this interval is αT:

$$i_{\rm Lc}(t_1) = i_{\rm Lc}(t_0) + \frac{(V_{\rm in} + V_o)\,\alpha T}{L_c} = 0. \tag{1}$$

State II [t_1, t_2]: At t_1, current is zero and D_{o1} cuts OFF, D_{o2} begins to freewheel current. Port *CD* is shorted through Q_6 and D_{o2}. State II is shown in Fig. 3(b):

$$i_{\rm Lc}(t_2) = \frac{V_{\rm in}(D_1 - \alpha)T}{L_c} = I_1. \tag{2}$$

State III [t_2, t_3]: At t_2, Q_6 turns OFF and Q_5 turns ON. The energy transfers from the input source port to the output load directly, as shown in Fig. 3(c). The clamped inductor current may increase or decrease linearly with different voltage gains *M*:

$$i_{\rm Lc}(t_3) = \frac{V_{\rm in}(D_1 - \alpha)T}{L_c} + \frac{(V_{\rm in} - V_o)D_2T}{L_c} = I_2. \tag{3}$$

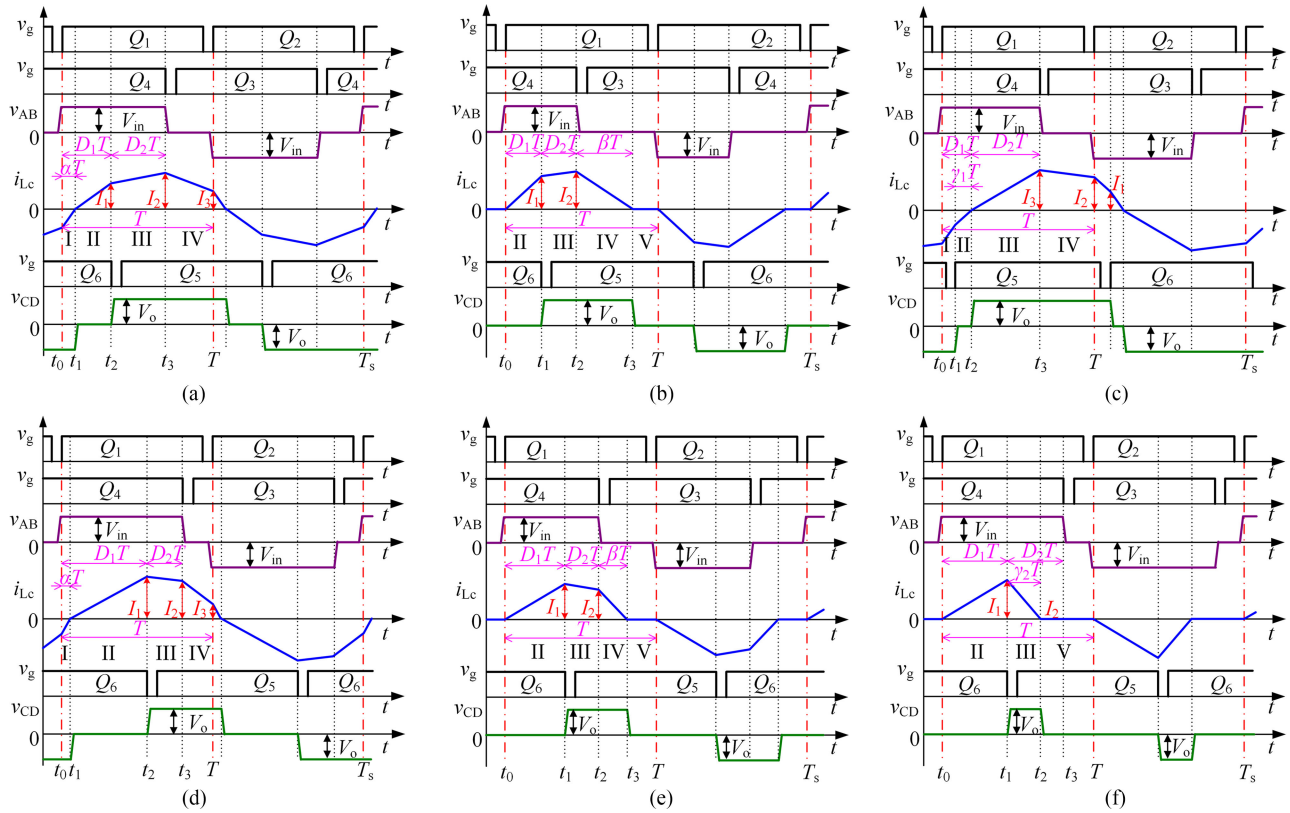

Fig. 2. Waveforms of the IBB converter. (a) Mode 1 at $M < 1$. (b) Mode 2 at $M < 1$. (c) Mode 3 at $M < 1$. (d) Mode 1 at $M > 1$. (e) Mode 2 at $M > 1$. (f) Mode 3 at $M > 1$.

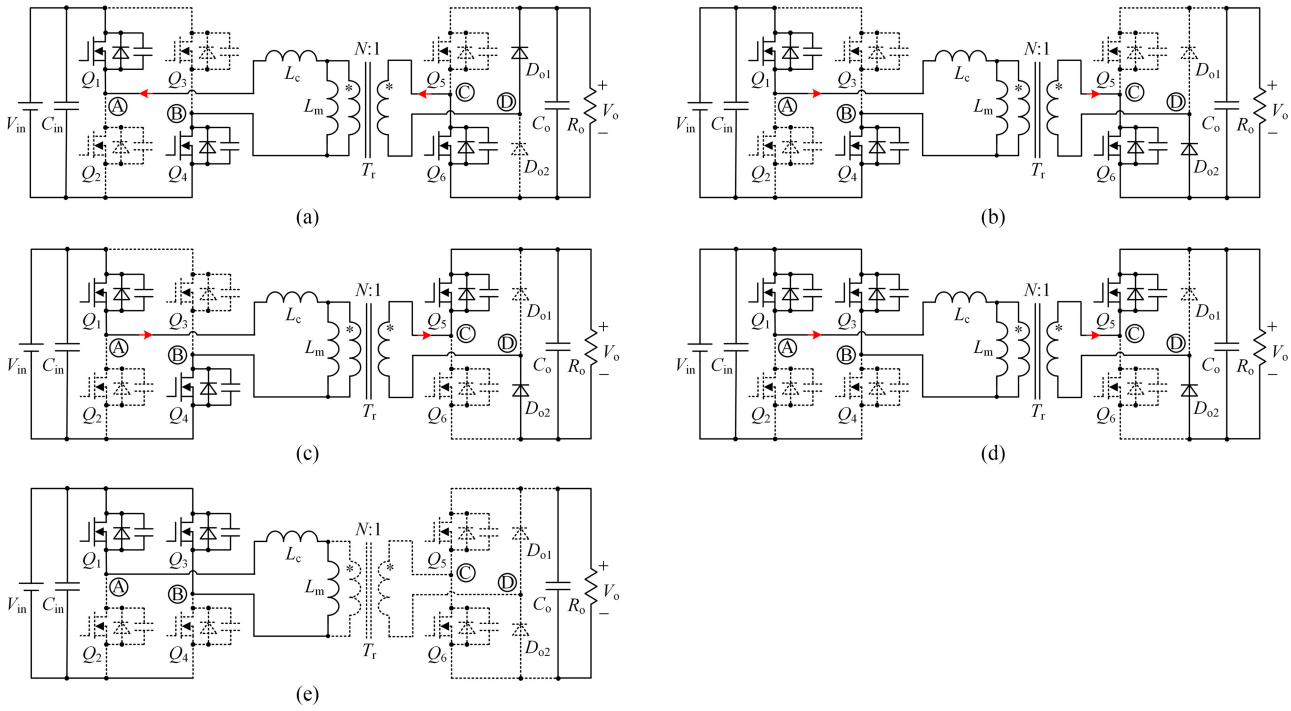

Fig. 3. Equivalent schematics in positive half-cycle. (a) State I. (b) State II. (c) State III. (d) State IV. (e) State V.

TABLE I
OUTPUT AVERAGE CURRENTS AT DIFFERENT MODES AND VOLTAGE GAINS

Mode	$M<1$	$M>1$
Mode 1	$I_o=\frac{V_oT}{2L_c}\frac{[M^2(2D_1-{D_1}^2-{D_2}^2-1)+(M+1)(4D_1+4D_2-3{D_1}^2-3{D_2}^2-2D_1D_2)]}{M(M+2)^2}$	
Mode 2	$I_o=\frac{V_oT}{2L_c}\frac{(D_1+D_2)^2-{D_2}^2M}{M^2}$	
Mode 3	$I_o=\frac{V_oT}{2L_c}\frac{[M^2(2D_2-{D_1}^2-{D_2}^2-1)+(M-1)(3{D_1}^2+3{D_2}^2+2D_1D_2-4D_1-4D_2)]}{M(M-2)^2}$	$I_o=\frac{V_oT}{2L_c}\frac{{D_1}^2}{M(M-1)}$

State IV [t_3, T]: At t_3, Q_4 turns OFF and Q_3 turns ON, so v_{AB} is zero. The current decreases linearly in Fig. 3(d):

$$i_{\mathrm{Lc}}(T)=I_2-\frac{V_o(1-D_1-D_2)T}{L_c}=I_3. \tag{4}$$

According to the operational principle of the transformer, the current values of the starting time and ending time of half-cycle are equivalent, and their directions are opposite. So α satisfies

$$\alpha=\frac{D_1M+D_1+D_2-M}{2+M}. \tag{5}$$

And the output average current is shown in Table I.

B. Mode 2

If the current decreases to zero before the end of half-cycle, the IBB converter is in DCM mode, shown as Fig. 2(b) and (e). The first three intervals of mode 2 are the same as states II–IV, and the last interval is state V, in which the current is zero, Q_2 and Q_3 are ON and v_{AB} is clamped to zero voltage level, as shown in Fig. 3(e). v_{CD} could be zero level in ideal case.

Assume βT as the length of the interval in which the current decreases from I_2 to zero, and

$$\beta=\frac{D_1+D_2}{M}-D_2. \tag{6}$$

The output current value of mode 2 is shown in Table I.

C. Mode 3

When $M<1$, at time t_2 (i.e., the end of state II) the current of the clamped inductor is still negative, shown in Fig. 2(c). The former interval of D_1T is state I. The latter interval of D_1T is state II with negative current, we define the interval length as γ_1T, and

$$\gamma_1=\frac{D_2-D_1-M}{2-M}. \tag{7}$$

When $M>1$, the current decreases to zero before the end of D_2T in Fig. 2(f). We define the interval length t_1 to zero current is γ_2T, and

$$\gamma_2=\frac{D_1}{M-1}. \tag{8}$$

The output current values of mode 3 are shown in Table I.

D. Summary

Above all, there are three different operational modes, and the boundary conditions are shown as following.

1) When $M<1$, the boundary condition between mode 1 and mode 3 satisfies

$$\gamma_1=\frac{D_2-D_1-M}{2-M}=0 \tag{9}$$

i.e.,

$$D_2=D_1+M. \tag{10}$$

The boundary condition between mode 1 and mode 2 satisfies

$$D_1+D_2+\beta=\frac{MD_1+D_1+D_2}{M}=1 \tag{11}$$

hence

$$D_2=M-(M+1)D_1. \tag{12}$$

Solving (10) and (12), we have $D_1=0$, $D_2=M$.

2) When $M>1$, the boundary condition between mode 1 and mode 2 satisfies

$$\alpha=\frac{D_1M+D_1+D_2-M}{(2+M)}=0 \tag{13}$$

i.e.,

$$D_2=M-(M+1)D_1. \tag{14}$$

The boundary condition between mode 2 and mode 3 satisfies

$$\gamma_2=\frac{D_1}{M-1}=D_2 \tag{15}$$

hence

$$D_1=(M-1)D_2. \tag{16}$$

Solving (14) and (16), we have $D_1=1-1/M$, $D_2=1/M$.

Usually, the current quantities are normalized by the base $I_{\mathrm{base}}=V/\omega L$. In this paper, we use $I_{\_\mathrm{base}}=V_oT/2L_c$ to normalize the above-mentioned formulae of output current, three-dimensional curves between D_1, D_2, and the output current are shown in Fig. 4, where *M* are 0.5, 0.8, 1.25, and 2.

From Fig. 4(a), when the output load current $I_o*=0.75$, there are a lot of combinations between D_1 and D_2. It is necessary to select the optimal variables combination of D_1 and D_2.

From Fig. 4, there is a maximum value of the output current in mode 1. Setting the partial derivatives of the output average current to zero, and

$$I_{o\_\max}=\frac{V_oT}{2L_c}\frac{(M+1)}{M(M^2+2M+2)} \tag{17}$$

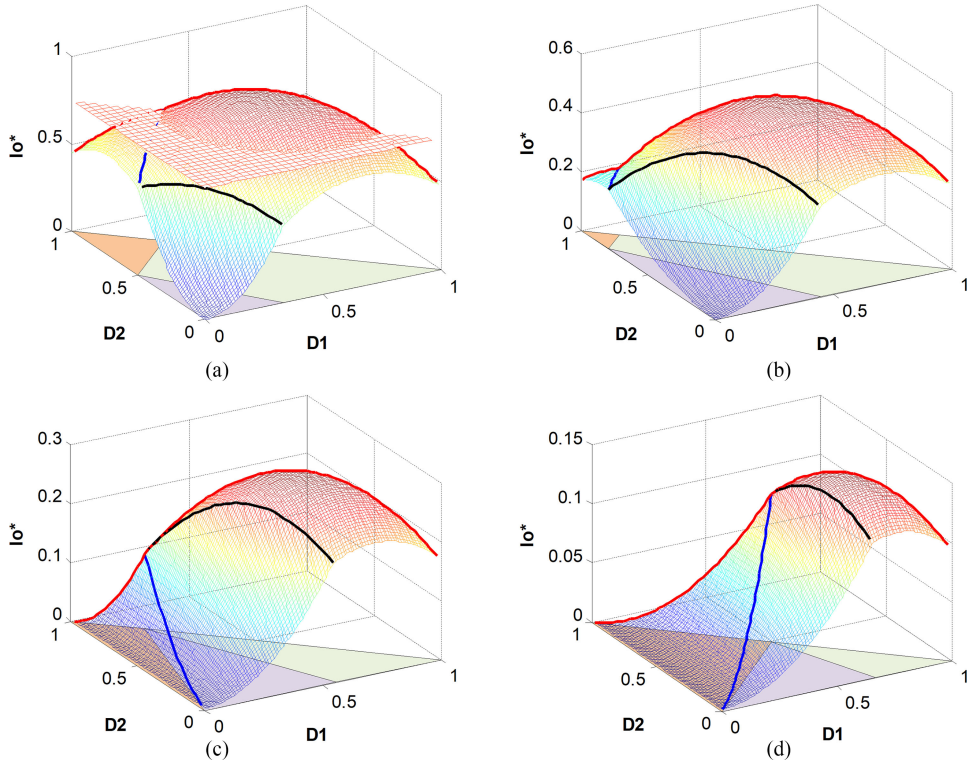

Fig. 4. Three-dimensional graphs of I_o* versus D_1 and D_2. (a) $M = 0.5$. (b) $M = 0.8$. (c) $M = 1.25$. (d) $M = 2$.

where

$$D_{1\_\max} = \frac{M^2 + M + 1}{M^2 + 2M + 2}, D_{2\_\max} = \frac{M + 1}{M^2 + 2M + 2} \quad (18)$$

satisfying

$$D_{1\_\max} + D_{2\_\max} = 1. \quad (19)$$

This result can be applied to both cases $M > 1$ and $M < 1$.

III. Criteria and Control Trajectories of Optimal Control Strategy

A. State of the Art

We draw the control trajectories of SPS and DPS control in Fig. 5 by setting D_1 as the variable of horizontal coordinate, and D_2 as the variable of vertical coordinate. The small dot represents the maximum output current point. Using the variables defined in this paper, SPS control trajectory can be described as $D_1 + D_2 = 1$. The start point of SPS control is $D_1 = 0$, $D_2 = 1$ at extreme light load, and the end point is the maximum output current point.

When $M > 1$, DPS control trajectory is the same as SPS control trajectory. When $M < 1$ in DPS control, at light load only D_2 is regulated and $D_1 = 0$, at heavy load $D_1 + D_2 = M$, D_1 and D_2 are regulated simultaneously. The start point of DPS control trajectory is $D_1 = 0$, $D_2 = 0$ with zero output power, but the end point is not the maximum output current point.

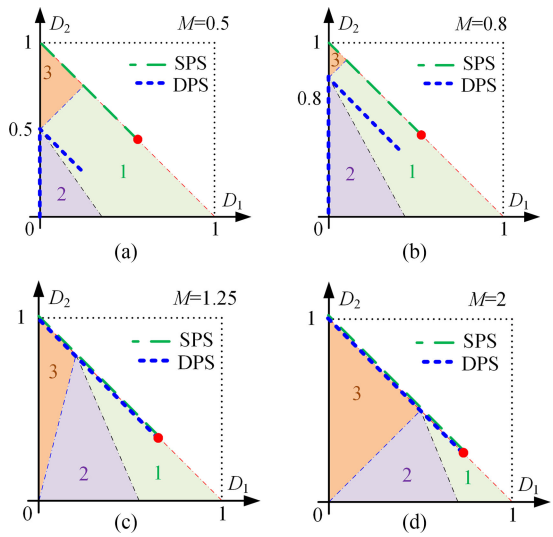

Fig. 5. Control trajectories of SPS and DPS control strategies. (a) $M = 0.5$. (b) $M = 0.8$. (c) $M = 1.25$. (d) $M = 2$.

B. Determination of Optimal Operating Point

The current of the clamped inductor is controllable by the voltage across it. It is observable and can reflect the current of transfer and power devices. Fig. 6 reveals the relationships between the normalized peak values and the normalized rms values of the current of the clamped inductor with the same I_o* by numerical calculation. Under the same input and output conditions, the lower peak current of the clamped inductor, the

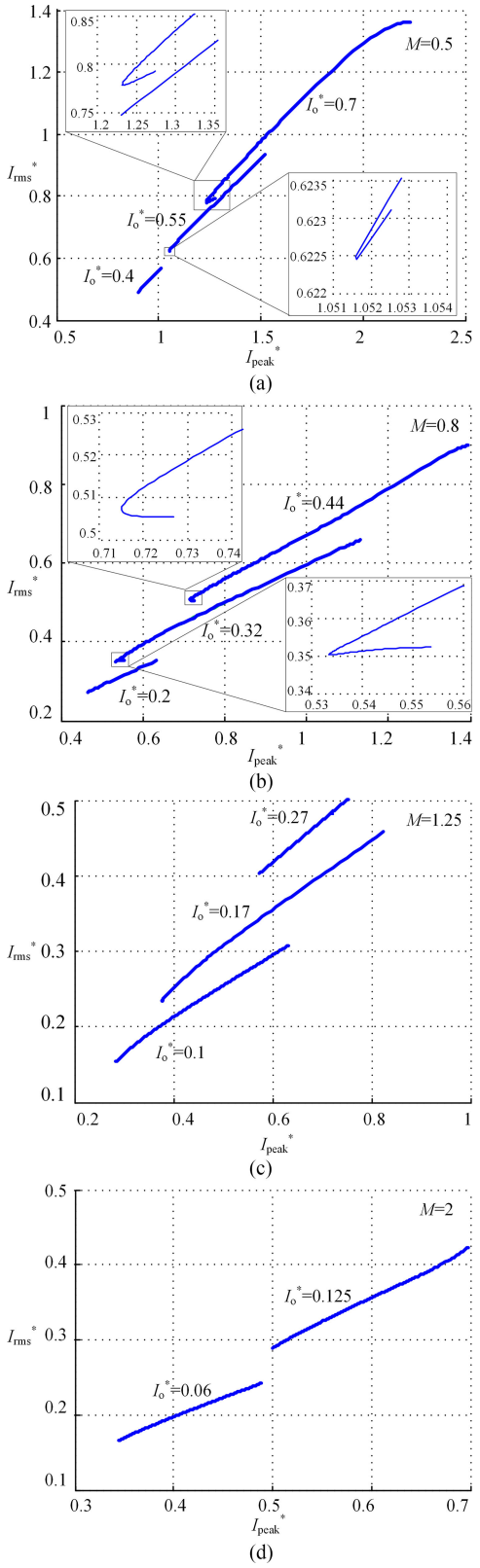

Fig. 6. Numerical solutions of rms current and peak current of a clamped inductor at different I_o^*. (a) $M = 0.5$. (b) $M = 0.8$. (c) $M = 1.25$. (d) $M = 2$.

lower rms current, the less conduction loss and switching loss of power devices, the less copper loss of transformer, and the lower circulating energy are observed, such that the efficiency

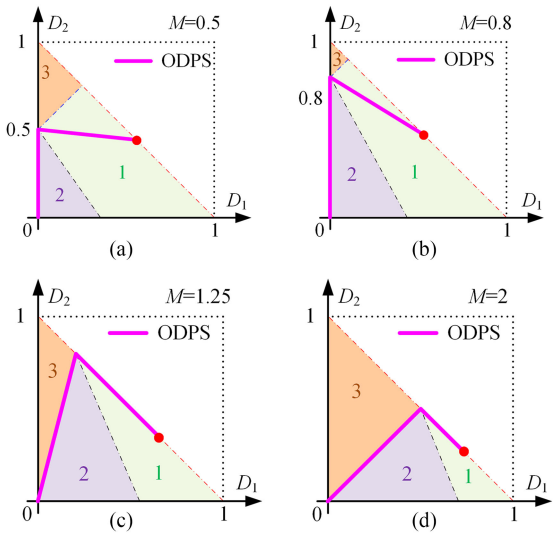

Fig. 7. Control trajectories of ODPS control strategy. (a) $M = 0.5$. (b) $M = 0.8$. (c) $M = 1.25$. (d) $M = 2$.

of the converter is higher. Although there is a little deviation when $M < 1$, but peak values and rms values are basically meet monotonous relations.

Therefore, we can use the peak current of the clamped inductor to determine the optimal operating point. The criteria of determining optimal operating point can be listed as

$$\begin{aligned} &\min : \text{peak value of } i_{\mathrm{Lc}} \\ &\text{s.t.} \quad \text{the same } M, I_o. \end{aligned} \tag{20}$$

Here, min means minimum, and s.t. means subject to.

When $M < 1$ at light load in mode 3, the circulating energy is large, the current stresses of the power devices increase, and the extra conduction loss declines the efficiency of the converter. When $M > 1$ at light load in mode 3, the current of the clamped inductor is zero in the latter interval of D_2T in Fig. 2(f). Parasitic components may resonant with each other in the nonideal case. As a result, we would like to set the operating point in mode 1 or mode 2.

C. Control Trajectories at $M < 1$

When $M < 1$, the peak current value appears at time t_3, i.e., I_2 at the end of state III. In mode 1

$$I_2 = \frac{V_o T}{2L_c} \frac{2\left[D_1 + M + \left(1 - M - M^2\right) D_2\right]}{M\left(2 + M\right)}. \tag{21}$$

In mode 2

$$I_2 = \frac{V_o T}{2L_c} \frac{2\left[D_1 + \left(1 - M\right) D_2\right]}{M}. \tag{22}$$

In mode 1, the optimal point is

$$D_2 = M - D_1 \frac{\left[\left(M^2 + 3M + 3\right)\left(M^2 + M - 1\right) + \left(M + 1\right)\right]}{\left[\left(M^2 + M - 1\right)\left(M + 1\right) + \left(M^2 + 3M + 3\right)\right]}. \tag{23}$$

In mode 2, the optimal point is

$$D_1 = 0. \tag{24}$$

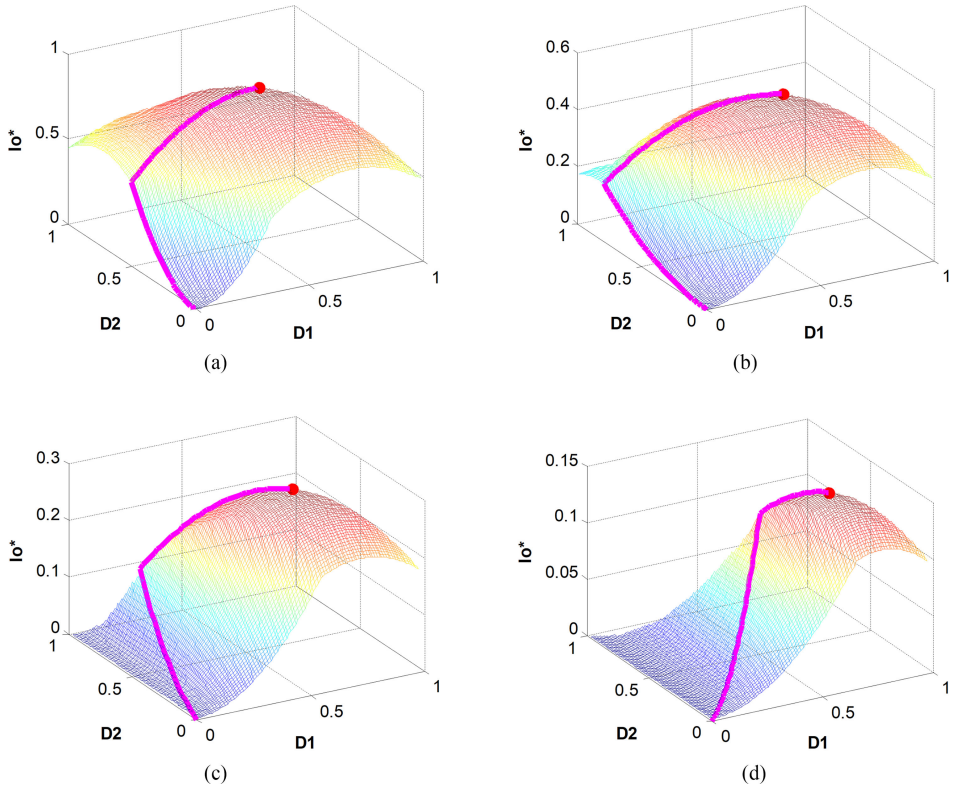

Fig. 8. ODPS control trajectories in three-dimensional graphs. (a) $M = 0.5$. (b) $M = 0.8$. (c) $M = 1.25$. (d) $M = 2$.

The ODPS control trajectory and three-dimensional curves between D_1, D_2, and the output current when $M < 1$ are shown in Figs. 7(a) and (b), and 8(a) and (b). The converter operates in mode 1 at heavy load, and in mode 2 at light load. The turning-point is $D_1 = 0$, $D_2 = M$. And the end of the optimal control trajectory is the maximum output power point.

D. Control Trajectories at $M > 1$

When $M > 1$, the peak current value appears at time t_2, i.e., I_1 at the end of state II. In mode 1

$$I_1 = \frac{V_o T}{2L_c} \frac{2\left(D_1 - D_2 + M\right)}{M\left(2 + M\right)}. \tag{25}$$

And the optimal point is

$$D_1 + D_2 = 1. \tag{26}$$

In mode 2, I_1 is

$$I_1 = \frac{V_o T}{2L_c} \frac{2D_1}{M}. \tag{27}$$

And the optimal point is

$$MD_2 - D_1 - D_2 = 0. \tag{28}$$

The ODPS control trajectory and three-dimensional curves between D_1, D_2, and output current when $M > 1$ are shown in Figs. 7(c) and (d), and 8(c) and (d). The converter operates in mode 1 at heavy load, with square voltage waveform of v_{AB}, and in mode 2 at light load. The turning-point is $D_1 = 1 - 1/M$, $D_2 = 1/M$. And the end of the optimal control trajectory is the maximum output power point. Like DPS control strategy, ODPS control strategy can also operate in whole load range.

Compared with SPS and DPS control strategy, ODPS control strategy has two differences, one is at heavy load when $M < 1$, and the other one is at light load when $M > 1$. In the former case, ODPS control trajectory is located between SPS and DPS, and there is no obvious difference among the three strategies. In the latter case, the three control strategies correspond to the same value of D_1 at the same output power, while the values of D_2 are different. SPD and DPS control trajectories are located on the line $D_1 + D_2 = 1$, v_{AB} is $\pm V_{\text{in}}$ without zero voltage level. Resonance may occur if the parasitic parameters are taken into consideration. The ODPS control trajectory is located on the boundary condition of mode 2 and mode 3, and the primary side switch turns OFF when the current drops to zero simultaneously. ODPS control strategy avoids the resonance between parasitic components.

When $M = 1$, the control trajectories are $D_2 = 0$ and $D_1 + D_2 = 1$. From Fig. 7, the converter can transit from buck mode to boost mode smoothly.

E. Soft-Switching Performance

When $M < 1$ at light load, $D_1 = 0$ and only D_2 is changed to regulate the output power, and the IBB converter is in DCM mode. ZVS ON of primary leading-legs Q_3 and Q_4 can be achieved easily. And zero current switching (ZCS) ON and ZCS OFF of primary lagging-legs Q_1, Q_2, secondary switches, and diodes are independent of the load power.

When $M < 1$ at heavy load, primary-side switches are all ZVS ON, secondary-side switches are ZVS ON, and secondary-side diodes shut OFF naturally.

When $M > 1$ at light load, the control trajectory is the boundary condition between mode 2 and mode 3. Thus, the converter is in DCM mode, and the inductor current decreases to zero exactly at the end of D_2T. Primary-side switches are all ZCS ON and OFF, and secondary-side switches are ZVS ON, secondary-side diodes shut OFF naturally.

When $M > 1$ at heavy load, $D_1 + D_2 = 1$, and Q_1 and Q_4, Q_2 and Q_3 turn ON and OFF at the same time. The soft-switching performance is same to that of heavy load when $M < 1$.

The converter is in DCM mode with no circulating energy at light load in ideal case. If we take magnetizing inductance and parasitic capacitances of secondary diodes into consideration, the switching current is no longer zero in nonideal case. The power devices are quasi-ZCS ON and OFF. However, the switching loss of quasi-ZCS is still small than that of hard switching. ZVS ON has less switching loss than quasi-ZCS ON, and ZVS ON needs larger circulating energy and has larger conduction loss than quasi-ZCS ON. There should be a trade-off between the switching loss and conduction loss. And the theoretical analysis of parasitic parameters and IBB converter efficiency need further study. The converter is in CCM mode at heavy load. The current of the clamped inductor in dead zone contains magnetizing current of transformer and the equivalent load current. It is easy to realize ZVS of switches in the converter. Above all, the converter has potential to achieve high efficiency.

IV. Parameter Design

The design considerations of the IBB converter contain the maximum load power, the range of input voltage, the turns ratio of transformer, switching frequency, and the value of the clamped inductor. Setting *M* in both buck and boost mode, i.e., $M_{\max} > 1$ and $M_{\min} < 1$, can improve the whole efficiency of the converter. The normalized output currents of the maximum point and the turning-point at different *M* of ODPS control strategy are shown in Fig. 9(a). The minimum output current value is zero, and we omit it here. The graph can be divided into several areas: impossible area, mode 2 with $D_1 = 0$ at $M < 1$, mode 1 at $M < 1$, mode 1 with $D_1 + D_2 = 1$ at $M > 1$, boundary between mode 2 and mode 3 at $M > 1$.

It is needed to make sure that the converter can output the rated load power. Draw I_o* to Fig. 9(a), it is a straight line which paralleled to the horizontal axis. The larger the I_o*, the higher the utilization of the converter, and the smaller the range of *M*, i.e., the smaller the range of input voltage. Therefore, there is a trade-off between I_o* and *M*. In this paper, we choose $I_o* = 0.2$, and the feasible range of *M* is [0.5, 1.6511].

Fig. 9(b) shows the normalized output currents of SPS and DPS control strategies. At $I_o* = 0.2$, $M = 0.7677$. This means the output power cannot be adjusted if $M < 0.7677$ under SPS control strategy. When $M < 1$, the maximum output current under DPS control is less than the maximum output point of the IBB converter, which has little impact on the converter

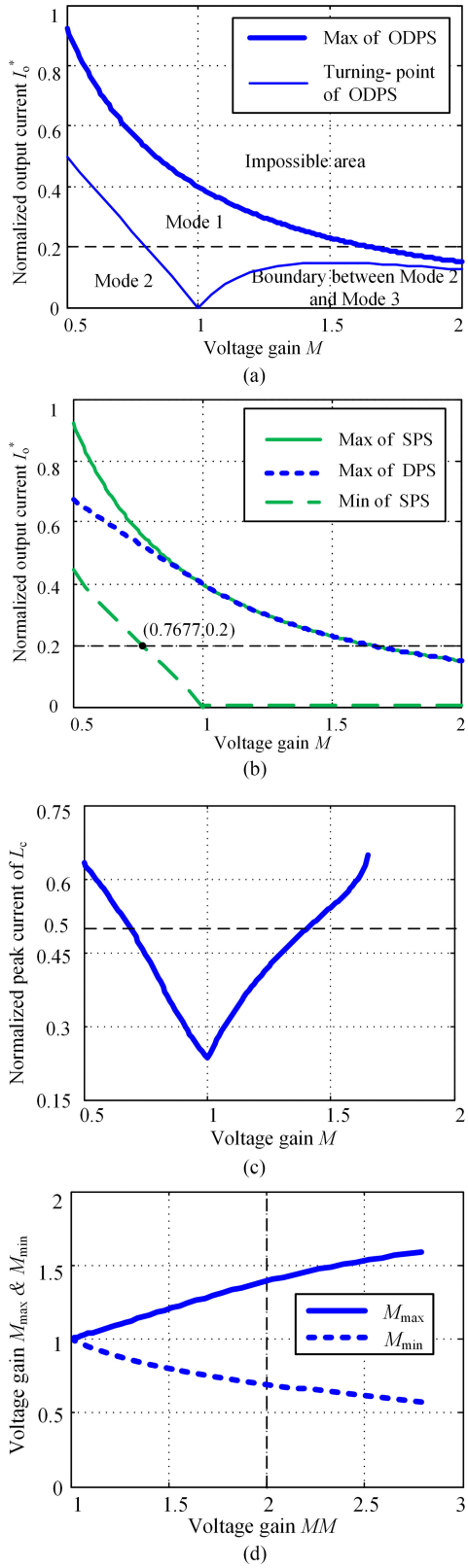

Fig. 9. Relationships between output current and peak current of a clamped inductor at different *M*. (a) The maximum output current and turning point output current of ODPS control strategy at different *M*. (b) The maximum and minimum output currents of SPS and DPS control strategies at different *M*. (c) Normalized peak current of a clamped inductor at different *M* with the same output current. (d) $M_{\max}$ and $M_{\min}$ versus *MM*.

TABLE II
PARAMETERS OF THE PROPOSED CONVERTER

Components	Parameters
Input voltage	100–200 V
Output voltage	380 V
Maximum output power	1000 W
Switching frequency	60 kHz
Turns ratio of transformer	14:38
Clamped inductor	19 μH
Primary-side MOSFETs Q_1 Q_2	IRFB4137PBF
Primary-side MOSFETs Q_3 Q_4	IPB200N25N3G
Secondary-side MOSFETs	IPB65R110CFD
Secondary-side diodes	16CDU06-M3

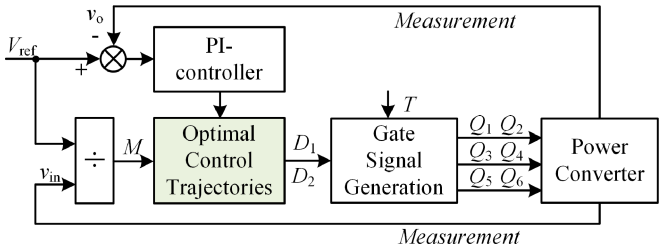

Fig. 10. Control block diagram of ODPS control strategy.

performance. When $M > 1$, the maximum and minimum output current values of the three control strategies are the same.

Fig. 9(c) shows the curve of the normalized peak current of the clamped inductor at rated load versus different M. When M is closer to 1, the peak value of the inductor current is smaller. When M is far away from 1, the peak value of the inductor current is bigger. Solve the two M values with the same peak current, and named as $M_{\max}$ and $M_{\min}$. Assume $MM = M_{\max}/M_{\min}$, the relationships among $M_{\max}$, $M_{\min}$, and MM is shown in Fig. 9(d).

The ratio between the maximum value and the minimum value of input voltage is MM. Then, $M_{\max}$ and $M_{\min}$ can be decided from Fig. 9(d). And we can calculate the turns ratio N of transformer based on the input voltage and output voltage and the range of M. Next, determine the value of the clamped inductor, by using the expressions $I_o* = 0.2$ and $I_{\_base} = V_o T/2L_c$. At last, the maximum peak current at rated load can be calculated, can be used to choose power devices.

V. EXPERIMENTAL VERIFICATION

A 1000 W prototype of the IBB converter with the clamped inductor is built to verify the feasibility of proposed optimal control strategy. The specifications are listed in Table II.

The control block diagram of ODPS control strategy is shown in Fig. 10. The difference between the reference voltage and the sampled output voltage is the input of PI controller. The input voltage of the IBB converter is sampled to calculate the value of M. Then the control trajectories can be calculated by (23), (24), (26), and (28). The output of PI-controller is the input of optimal control strategies block, and it decides the operating point of the control trajectories, i.e., the values of control variables D_1 and D_2. After gate signal generation block, D_1 and D_2 are transferred to the gate signals of switches. The control loop is very simple and can be implemented by digital signal processor easily.

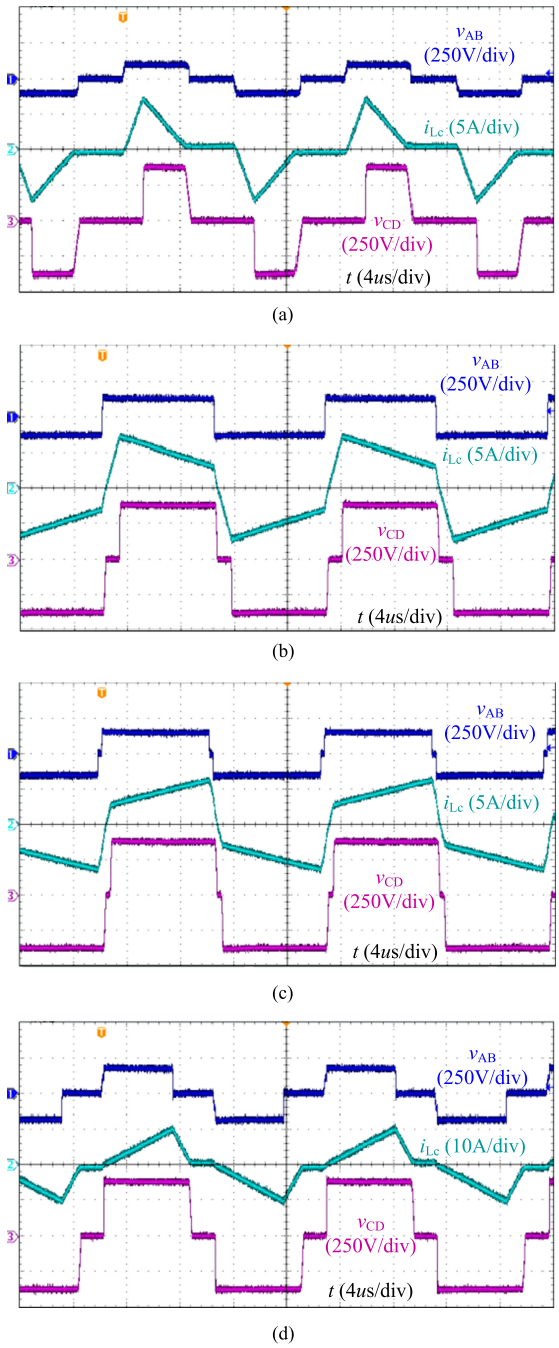

Fig. 11. Experimental waveforms at different operational areas of ODPS control strategy (a) $V_{\text{in}} = 100$ V, $P_o = 200$ W. (b) $V_{\text{in}} = 130$ V, $P_o = 600$ W. (c) $V_{\text{in}} = 150$ V, $P_o = 600$ W. (d) $V_{\text{in}} = 180$ V, $P_o = 600$ W.

Fig. 11 shows the experimental waveforms in different modes. If dead time and parasitic parameters are taken into consideration, there is a slight deviation between the calculation results and theoretical values of ODPS control strategy. However, the converter maintains high efficiency because the actual operating point is in the vicinity of optimal point.

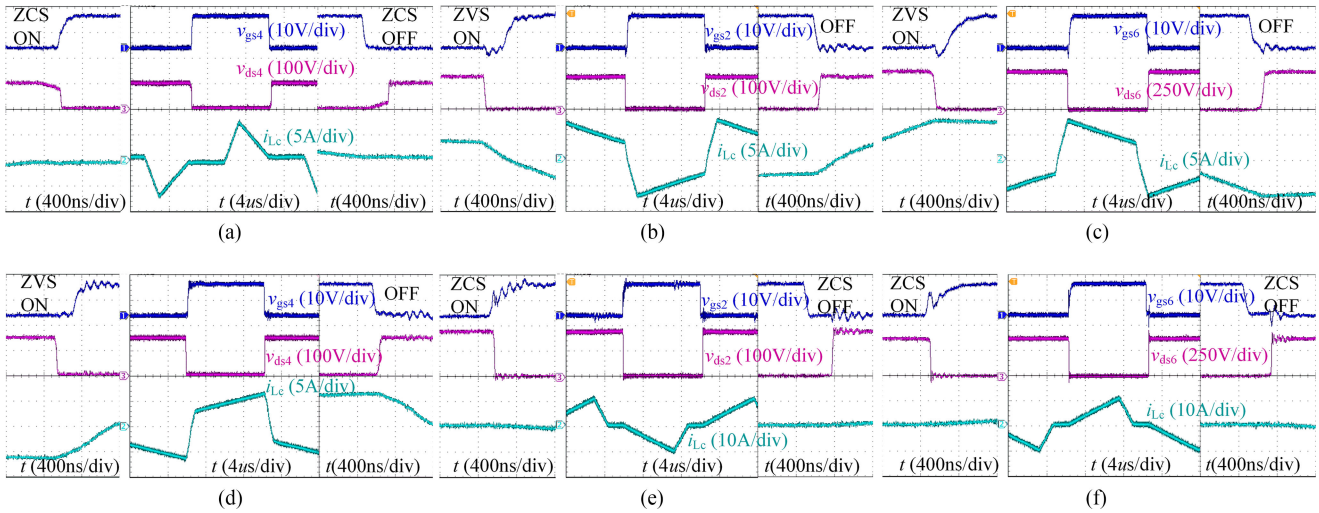

Fig. 12. Switching waveforms of Q_2, Q_4, and Q_6 in different modes. (a) Q_4 $V_{\rm in}$ = 100 V, P_o = 200 W. (b) Q_2 $V_{\rm in}$ = 130 V, P_o = 600 W. (c) Q_6 $V_{\rm in}$ = 130 V, P_o = 600 W (d) Q_4 $V_{\rm in}$ = 150 V, P_o = 600 W. (e) Q_2 $V_{\rm in}$ = 180 V, P_o = 600 W. (f) Q_6 $V_{\rm in}$ = 180 V, P_o = 600 W.

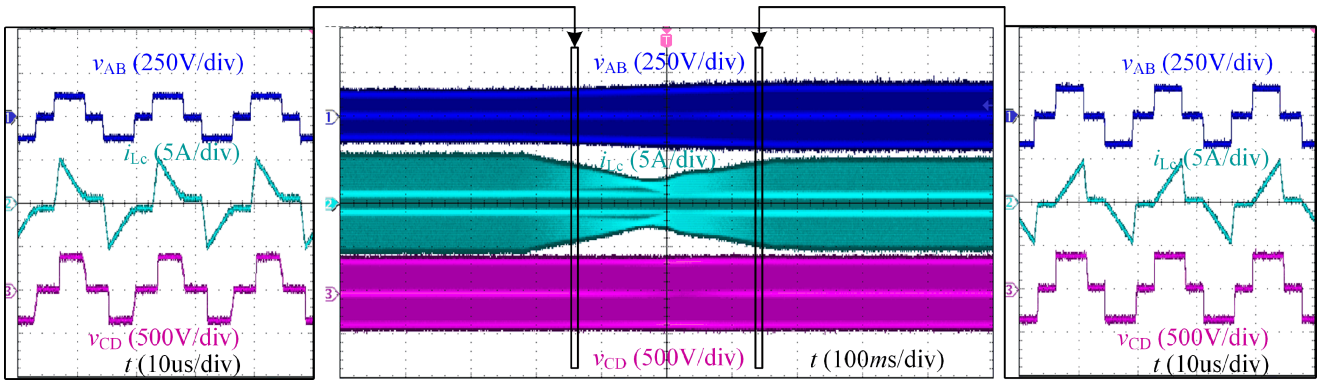

Fig. 13. Experimental waveforms of modes transition.

The soft-switching waveforms of the primary-side and secondary-side switches under different operation modes are shown in Fig. 12. $v_{\rm gs2}$, $v_{\rm gs4}$, and $v_{\rm gs6}$ are the driving voltages of the switches Q_2, Q_4, and Q_6, while $v_{\rm ds2}$, $v_{\rm ds4}$, and $v_{\rm ds6}$ are corresponding drain–source voltages. ZVS ON, quasi-ZCS ON and OFF can be achieved for the primary-side and secondary-side switches in both buck and boost mode.

The mode transition waveforms are shown in Fig. 13. The mode transition is triggered by changing the input voltage from 120 to 160 V at 200 W load power. The peak inductor current first becomes smaller, and then gets bigger along with the increase of input voltage. It can be seen that smooth mode transition between boost mode and buck mode is achieved.

Fig. 14(a) shows test under 100 V input voltage and 200 W output power of the IBB converter under DPS control strategy. The leakage inductance and parasitic capacitors of diodes are resonant, which damages the electromagnetic compatibility of the converter. And the circulating current generated by the magnetizing inductance of transformer is bigger than that of Fig. 11(a). Fig. 14(b) shows test under 150 V voltage and 600 W output power under DPS control strategy. The difference between Fig. 11(c) and Fig. 14(b) is very small. At heavy load when $M > 1$ and light load when $M < 1$, the experimental waveforms under DPS control strategy are the same as that of ODPS control strategy, shown as Fig. 11(b) and (d).

The efficiency comparison between DPS and ODPS control strategies versus output power at different input voltages is shown in Fig. 15. And at light load when the input voltage is 110 and 130 V, $M > 1$, the efficiency under DPS control strategy is less than that of ODPS control strategy because of the magnetizing and leakage inductance of the transformer. At heavy load when the input voltage is 170 V, $M < 1$, the control trajectories of the two control strategies are close, and the efficiency curves are basically in coincidence in Fig. 15. DPS and ODPS control strategies both can achieve the soft-switching of power devices and high efficiency of the converter.

The curves for efficiency versus output power under 100, 120, 140, 160, and 200 V input voltages of ODPS control strategy are presented in Fig. 16(a). When the input voltage is 100 and 120 V, the converter operates in boost mode. When the input voltage is 160 and 200 V, the converter operates in buck mode. When the input voltage is 140 V, the converter operates in balance mode,

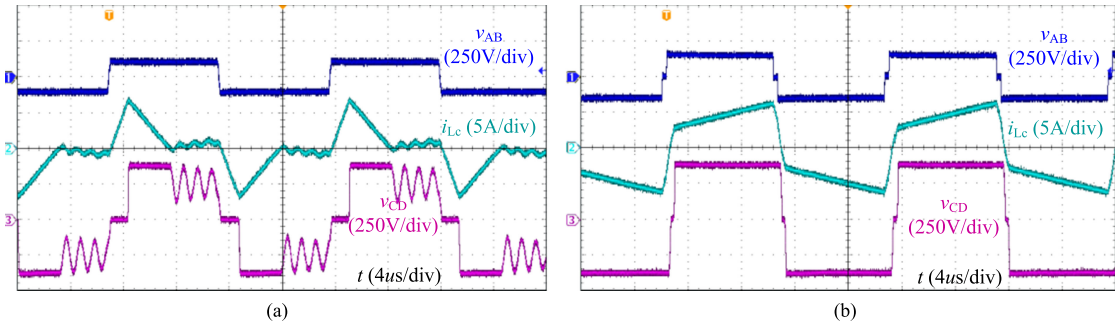

Fig. 14. Experimental waveforms of DPS control strategy. (a) $V_{\rm in} = 100$ V, $P_o = 200$ W. (c) $V_{\rm in} = 150$ V, $P_o = 600$ W.

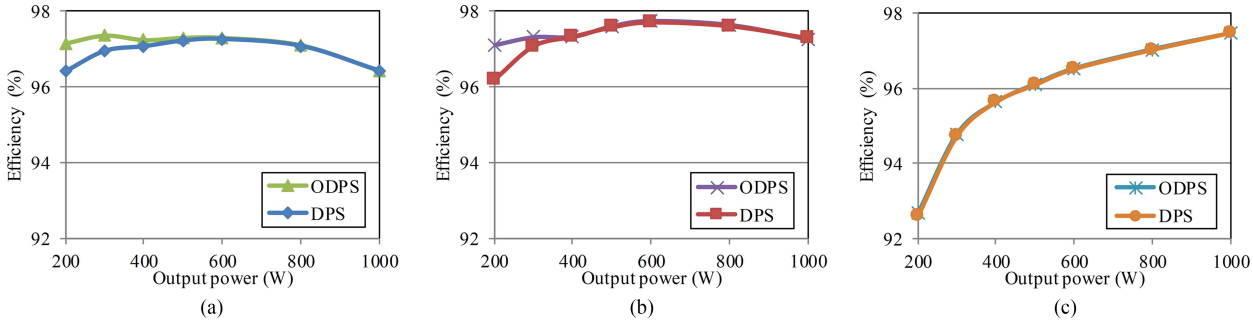

Fig. 15. Efficiency comparison between ODPS and DPS control strategies versus output power. (a) $V_{\rm in} = 110$ V. (b) $V_{\rm in} = 130$ V. (c) $V_{\rm in} = 170$ V.

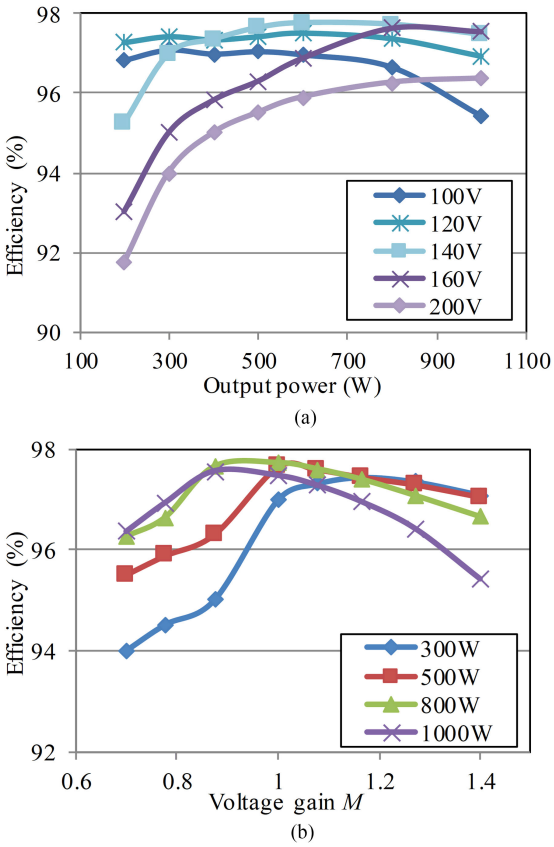

Fig. 16. Efficiency curves of ODPS control strategy. (a) Efficiency curves versus output power at different input voltages. (b) Efficiency curves versus voltage gain at different output powers.

and the peak efficiency of the IBB converter is about 97.76% at 600 W output power. The measured efficiency curves with respect to different voltage gain M at different output powers are shown in Fig. 16(b). It can be seen that the highest efficiency is achieved when the voltage gain M is near 1. When the output power is 800 and 1000 W, the peak efficiency appears at $M < 1$. That is because the conduction loss increases significantly at heavy load. When the output power is 300 W, the peak efficiency appears at $M > 1$. That is because the switching loss is playing a dominant role in the whole converter efficiency. The range of input voltage is 100–200 V, and voltage gain $M_{\rm max}/M_{\rm min} = 2$. The experimental results indicate that high efficiency over a wide input voltage range has been achieved with the proposed ODPS control strategy.

VI. Conclusion

An ODPS control strategy of the IBB converter has been proposed and investigated in this paper. The analysis is straightforward by using the two control variables D_1 and D_2, and the three-dimensional graphs of the output current. The current of the clamped inductor of ac link reflects the performance of the IBB converter, and has been used to determine the optimal operating point and design the parameters. The optimal control strategy is easy to implement. Meanwhile, the power transfer capability and current stresses of the IBB converter are revealed. Moreover, the parameter design method takes all of the parameters into account. The analysis and performance have been fully validated experimentally on a 100–200 V-input, 380 V-output hardware prototype. The results demonstrate that the IBB con-

verter can operate in a wide range of input voltage, and can transit from boost mode to buck mode smoothly.

In this paper, we have improved the theoretical analysis of dual-phase-shift control of the IBB converter, and proposed the determination method of optimal operation point. The ODPS control strategy can be applied to the other derivations of IBB converter family.

REFERENCES

[1] B. Y. Chen and Y. S. Lai, "Switching control technique of phase-shift-controlled full-bridge converter to improve efficiency under light-load and standby conditions without additional auxiliary components," *IEEE Trans. Power Electron.*, vol. 25, no. 4, pp. 1001–1012, Apr. 2010.

[2] X. Ruan and Y. Yan, "Soft-switching techniques for PWM full bridge converters," in *Proc. 2000 IEEE 31st Annu. Power Electron. Spec. Conf.*, vol. 2, Galway, 2000, pp. 634–639.

[3] X. Fang, H. Hu, Z. J. Shen, and I. Batarseh, "Operation mode analysis and peak gain approximation of the LLC resonant converter," *IEEE Trans. Power Electron.*, vol. 27, no. 4, pp. 1985–1995, Apr. 2012.

[4] G. Ivensky, S. Bronshtein, and A. Abramovitz, "Approximate analysis of resonant LLC dc-dc converter," *IEEE Trans. Power Electron.*, vol. 26, no. 11, pp. 3274–3284, Nov. 2011.

[5] C. Yao, X. Ruan, and X. Wang, "Automatic mode-shifting control strategy with input voltage feed-forward for full-bridge-boost dc–dc converter suitable for wide input voltage range," *IEEE Trans. Power Electron.*, vol. 30, no. 3, pp. 1668–1682, Mar. 2015.

[6] C. Yao, X. Ruan, X. Wang, and C. K. Tse, "Isolated buck–boost dc/dc converters suitable for wide input-voltage range," *IEEE Trans. Power Electron.*, vol. 26, no. 9, pp. 2599–2613, Sep. 2011.

[7] Y. Lu, H. Wu, K. Sun, and Y. Xing, "A family of isolated buck-boost converters based on semiactive rectifiers for high-output voltage applications," *IEEE Trans. Power Electron.*, vol. 31, no. 9, pp. 6327–6340, Sep. 2016.

[8] H. Wu, Y. Lu, K. Sun, and Y. Xing, "Phase-shift-controlled isolated buck-boost converter with active-clamped three-level rectifier (ac-TLR) featuring soft-switching within wide operation range," *IEEE Trans. Power Electron.*, vol. 31, no. 3, pp. 2372–2386, Mar. 2016.

[9] H. Wu, T. Mu, H. Ge, and Y. Xing, "Full-range soft-switching-isolated buck-boost converters with integrated interleaved boost converter and phase-shifted control," *IEEE Trans. Power Electron.*, vol. 31, no. 2, pp. 987–999, Feb. 2016.

[10] I. D. Jitaru, "A 3 kW soft switching dc-dc converter," in *Proc. 15th Annu. IEEE Appl. Power Electron. Conf. Expo.*, vol. 1, New Orleans, LA, 2000, pp. 86–92.

[11] D. S. Gautam, F. Musavi, W. Eberle, and W. G. Dunford, "A zero-voltage switching full-bridge dc–dc converter with capacitive output filter for plug-in hybrid electric vehicle battery charging," *IEEE Trans. Power Electron.*, vol. 28, no. 12, pp. 5728–5735, Dec. 2013.

[12] C. Zhao, X. Wu, P. Meng, and Z. Qian, "Optimum design consideration and implementation of a novel synchronous rectified soft-switched phase-shift full-bridge converter for low-output-voltage high-output-current applications," *IEEE Trans. Power Electron.*, vol. 24, no. 2, pp. 388–397, Feb. 2009.

[13] J. Sun, G. K. Schoneman, and D. E. Jenkins, "Small-signal characterization of a zero-voltage switching dc/dc converter for pulse-load applications," in *Proc. 30th Annu. IEEE Power Electron. Spec. Conf.*, vol. 1, Charleston, SC, 1999, pp. 439–444.

[14] M. P. Meng, X. Wu, C. Zhao, J. Zhang, and Z. Qian, "A novel variable frequency soft switching full-bridge dc/dc converter with critical continuous mode control, " *Proc. CSEE*, vol. 32, no. 6, pp. 106–112, Feb. 2012.

[15] F. Krismer, S. Round, and J. W. Kolar, "Performance optimization of a high current dual active bridge with a wide operating voltage range," in *Proc. 2006 37th IEEE Power Electron. Spec. Conf.*, Jun. 2006, pp. 1–7.

[16] Y. Shen, X. Sun, W. Li, X. Wu, and B. Wang, "A modified dual active bridge converter with hybrid phase-shift control for wide input voltage range," *IEEE Trans. Power Electron.*, vol. 31, no. 10, pp. 6884–6900, Oct. 2016.

[17] Y. Wang, S. W. H. de Haan, and J. A. Ferreira, "Optimal operating ranges of three modulation methods in dual active bridge converters," in *Proc. 2009 IEEE 6th Int. Power Electron. Motion Control Conf.*, Wuhan, 2009, pp. 1397–1401.

[18] F. Krismer and J. W. Kolar, "Efficiency-optimized high-current dual active bridge converter for automotive applications," *IEEE Trans. Ind. Electron.*, vol. 59, no. 7, pp. 2745–2760, Jul. 2012.

[19] G. Oggier, G. O. García, and A. R. Oliva, "Modulation strategy to operate the dual active bridge dc-dc converter under soft switching in the whole operating range," *IEEE Trans. Power Electron.*, vol. 26, no. 4, pp. 1228–1236, Apr. 2011.

[20] B. Zhao, Q. Yu, and W. Sun, "Extended-phase-shift control of isolated bidirectional dc–dc converter for power distribution in microgrid," *IEEE Trans. Power Electron.*, vol. 27, no. 11, pp. 4667–4680, Nov. 2012.

[21] J. Zhang, F. Zhang, X. Xie, D. Jiao, and Z. Qian, "A novel ZVS dc/dc converter for high power applications," *IEEE Trans. Power Electron.*, vol. 19, no. 2, pp. 420–429, Mar. 2004.

[22] S. Kulasekaran and R. Ayyanar, "Analysis, design, and experimental results of the semidual-active-bridge converter," *IEEE Trans. Power Electron.*, vol. 29, no. 10, pp. 5136–5147, Oct. 2014.

[23] T. Mu, H. Wu, H. Liu, Y. Lu, and Y. Xing, "Dual-phase-shifted controlled isolated buck-boost converter with wide voltage-gain employing built-in boost cell," *Proc. CSEE*, vol. 35, no. 23, pp. 6105–6112, Dec. 2015.

[24] H. Wu, Y. Lu, T. Mu, and Y. Xing, "A family of soft-switching dc-dc converters based on a phase-shift-controlled active boost rectifier," *IEEE Trans. Power Electron.*, vol. 30, no. 2, pp. 657–667, Feb. 2015.

Fang Li was born in Hebei Province, China, in 1988. She received the B.S. degree from China University of Petroleum, Dongying, China, in 2010, She received the M.S. degree from Beijing Jiaotong University, Beijing, China, in 2012, she is currently working toward the Ph.D. degree in Beijing Jiaotong University, all in electrical engineering.

Her research interests include spacecraft power systems and high-frequency soft-switching dc/dc converters.

Yan Li (M'08) was born in Heilongjiang Province, China, in 1977. She received the B.S. and M.S. degrees from Yanshan University, Qinhuangdao, China, in 1999 and 2003, respectively, and the Ph.D. degree from the Nanjing University of Aeronautics and Astronautics, Nanjing, China, in 2009, all in electrical engineering.

From 1999 to 2009, she was with Yanshan University. In 2009, she joined the Faculty of Electrical Engineering, Beijing Jiaotong University, Beijing, China, where she is currently an Associated Professor in the College of Electrical Engineering. She was a Visiting Scholar in the Bradley Department of Electrical and Computer Engineering, Virginia Tech. Her current research interests include multiple-input dc/dc converters, renewable power systems, PV grid-tied system, and application of wide bandgap power semiconductor devices.

Xiaojie You was born in Fujian Province, China, in 1964. He received the M.S. degree from the China Agricultural University, Beijing, China, in 1989, and the Ph.D. degree from the Czech Technical University, Prague, Czech Republic, in 2001, both in electrical engineering.

He is a Professor and also the Director of the Power Electronic Research Institute, School of Electrical Engineering, Beijing Jiaotong University, Beijing, China. His current research interests include ac drive electric locomotive control, switching power control, active power filters, and power quality control.